

Ti-Exchanged UiO-66-NH₂-Containing Polyamide Membranes with Remarkable Cation Permselectivity

Tingting Xu¹, Fangmeng Sheng¹, Bin Wu², Muhammad Aamir Shehzad³, Aqsa Yasmin¹, Xiuxia Wang¹, Yubin He⁴, Liang Ge⁴, Xusheng Zheng¹, and Tongwen Xu⁴

¹University of Science and Technology of China

²Anhui University

³CAS Key Laboratory of Soft Matter Chemistry, Laboratory of Functional Membranes

⁴University of Sci. and Tech. of China

June 12, 2020

Abstract

Monovalent cation permselective membranes (MCPMs) are highly desirable for the extraction of Li⁺ and Na⁺ ions from earth-abundant sources, such as salt lakes and seawater. Metal-organic frameworks (MOFs) are promising functional nanomaterials with excellent potential for ion separation technologies owing to their regular structure and tunable pore sizes. However, the successful use of MOFs in ion separation membranes is still challenging owing to the numerous difficulties in preparing ultrathin and defect-free MOF membranes. Here, we proposed a facile post-synthetic method for the preparation of UiO-66(Zr/Ti)-NH₂ and subsequently immobilized UiO-66(Zr/Ti)-NH₂ in an ultrathin polyamide layer (~100 nm). The resulting thin-film nanocomposite membranes presented high monovalent cation permeation and excellent selectivity for mono-/di-valent cations. The $P_{\text{Na}^+/\text{Mg}^{2+}}$ and $P_{\text{Li}^+/\text{Mg}^{2+}}$ permselectivities of the best-performing thin-film nanocomposite membrane were 13.44 and 11.38, respectively, which were 3.8 and 5.1 times higher, respectively, than those of the commercial state-of-art CSO membrane.

Abstract

Monovalent cation permselective membranes (MCPMs) are highly desirable for the extraction of Li⁺ and Na⁺ ions from earth-abundant sources, such as salt lakes and seawater. Metal-organic frameworks (MOFs) are promising functional nanomaterials with excellent potential for ion separation technologies owing to their regular structure and tunable pore sizes. However, the successful use of MOFs in ion separation membranes is still challenging owing to the numerous difficulties in preparing ultrathin and defect-free MOF membranes. Here, we proposed a facile post-synthetic method for the preparation of UiO-66(Zr/Ti)-NH₂ and subsequently immobilized UiO-66(Zr/Ti)-NH₂ in an ultrathin polyamide layer (~100 nm). The resulting thin-film nanocomposite membranes presented high monovalent cation permeation and excellent selectivity for mono-/di-valent cations. The $P_{\text{Na}^+/\text{Mg}^{2+}}$ and $P_{\text{Li}^+/\text{Mg}^{2+}}$ permselectivities of the best-performing thin-film nanocomposite membrane were 13.44 and 11.38, respectively, which were 3.8 and 5.1 times higher, respectively, than those of the commercial state-of-art CSO membrane.

Keywords: metal-organic frameworks; post-synthetic; ion separation; interfacial polymerization; thin-film nanocomposite membranes

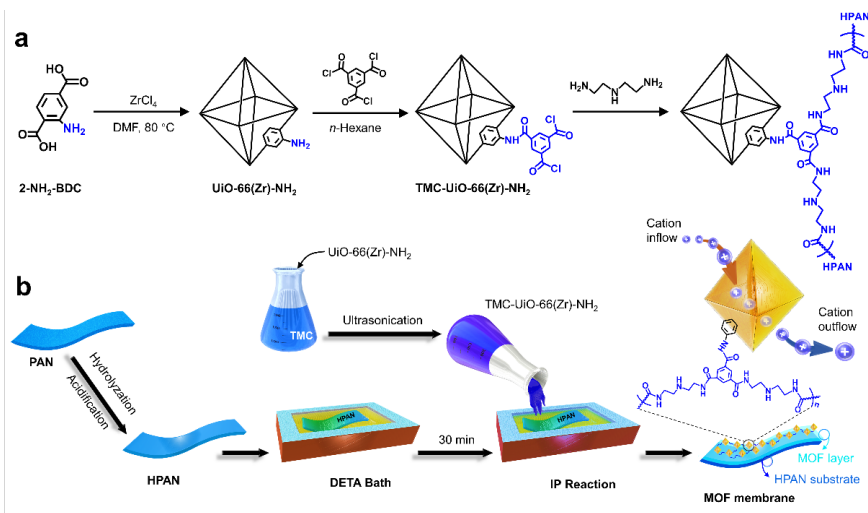
1. Introduction

The efficient extraction and permselective separation of valuable metal cations, such as Li⁺ and Na⁺, from salt lakes and seawater are critical aspects in membrane research and should be promptly addressed.^{1, 2} Recently, monovalent cation permselective membranes (MCPMs) have been widely investigated for cation

separation owing to their facile scalability and low energy consumption. Changing the electrostatic repulsive forces via the surface modification of the cation exchange membranes is the most common approach used to fabricate efficient MCPMs.^{3, 4} However, the complex surface modification methods and poor long-term stability of the deposited surface layers are drawbacks of MCPMs. In addition, the ion separation performance of MCPMs is hindered by the tradeoff between ion permeation and permselectivity. Another feasible approach for achieving high permeation and permselectivity is the incorporation of nanopores in membrane matrices to facilitate ion sieving.^{5, 6} However, the pores generated using traditional chemical reactions, such as chemical crosslinking⁷ and acid-base reactions⁸, or crystallinity adjustments⁹ are typically not uniform, and thus, inhibit the improvements in ion permeation and permselectivity. The shortcomings of the current MCPMs have dictated the need for more facile methods for the fabrication of high-performance permselective membranes. Such methods should facilitate both the size-sieving and ion-charge separation mechanisms, which are governed by the pore geometry and electrostatic forces, respectively, for fast ion permeation and high membrane permselectivity.¹⁰⁻¹²

Metal-organic frameworks (MOFs), a class of porous crystalline materials that consist of metal ions or clusters connected with organic ligands, present great potential for ion separation owing to their well-ordered and subnanometer-sized pores.¹³⁻¹⁵ However, the applications of MOFs for membranes, and in particular for ion separation, are limited owing to several challenges, including the preparation of ultrathin and defect-free MOF membranes.^{16, 17} Nevertheless, several researchers have described the deposition of phase-pure MOFs on inorganic substrates or porous polymer supports and have reported fabricating membranes with good ion separation performance.¹⁸⁻²² However, the complexity of the fabrication process of phase-pure MOF membranes and quick propagation of cracks owing to their brittleness limit their large-scale applications.²³ Moreover, the poor compatibility between MOFs and their polymer supports further induced unavoidable intrinsic instability in MOF-containing membranes.²⁴⁻²⁷

Given all the drawbacks of MCPMs and concerns associated with the use of MOFs for membranes, we hereby proposed a facile method for the fabrication of efficient and durable MCPMs using UiO-66(Zr)-NH₂ and a polyamide (PA) layer. We selected UiO-66(Zr)-NH₂ owing to its high water stability and tunable angstrom-scale pore size, which matches the diameters of the hydrated Li⁺ (0.76 nm), Na⁺ (0.72 nm), and Mg²⁺ (0.86 nm) ions well.²⁸ Hydrolyzed polyacrylonitrile (HPAN) was used as the substrate owing to its negligible ion transport resistance.²⁹ In this study, UiO-66(Zr)-NH₂ nanoparticles were prepared by reacting zirconium (IV) chloride (ZrCl₄) with 2-aminoterephthalic acid (2-NH₂-BDC). Subsequently, a fraction of the Zr⁴⁺ ions in UiO-66(Zr)-NH₂ was replaced with Ti³⁺ ions, which neutralized some of the positive charge and introduced a negative charge in the porous framework of UiO-66(Zr)-NH₂. The obtained product will hereafter be denoted as UiO-66(Zr/Ti)-NH₂. The facile post-synthetic method could promote the fast transportation of ions through the pores of UiO-66(Zr/Ti)-NH₂. Following interfacial polymerization (IP), the acyl chloride groups of trimesoyl chloride (TMC) reacted with UiO-66(Zr/Ti)-NH₂ and diethylenetriamine (DETA), as illustrated in Scheme 1a (where we used UiO-66(Zr)-NH₂ as an example), and produced a uniform polyamide layer that contained embedded MOF nanoparticles (Scheme 1b). Briefly, the prepared ultra-thin (~100 nm) MOF surface layers that contained ion transfer channels could simultaneously increase cation permeation and selectivity, and thus, circumvented the tradeoff between ion permeation and permselectivity. The proposed metal ion replacement strategy could further guide the membrane design and facilitate charge regulation for the subnanometer-sized pores of many MOFs that could be used for MOF-containing membranes for ion separation purposes. The method proposed for the fabrication of thin-film nanocomposite (TFN) membranes is described below. Moreover, the electrochemical properties and separation performance of the membranes were analyzed in detail, and were further compared with those of the commercial CSO membrane.



Scheme 1. (a) Reaction sequence for the synthesis of UiO-66(Zr)-NH₂ and trimesoyl chloride (TMC)-functionalized UiO-66(Zr)-NH₂ nanoparticles. (b) Schematic diagram for the fabrication of thin-film nanocomposite (TFN) membranes via the covalent bonding between metal-organic frameworks (MOFs) and TMC (UiO-66(Zr)-NH₂ was used as an example of MOF). Here 2-NH₂-BDC, DMF, PAN, HPAN, DETA, and IP denote 2-aminoterephthalic acid, N,N-dimethylformamide, polyacrylonitrile, hydrolyzed polyacrylonitrile, diethylenetriamine, and interfacial polymerization, respectively.

2. Experiments and Methods

2.1. Materials

ZrCl₄ (98%) and 2-NH₂-BDC (98%) were purchased from Shanghai Macklin Biochemical Co., Ltd. (Shanghai, China). TMC (98%) was purchased from Shanghai Energy Chemical Co., Ltd. (Shanghai, China). N,N-Dimethylformamide (DMF, 99.5%), hydrochloric acid (HCl, 36.0%), ethanol (C₂H₅OH, 99.7%), trichloromethane (CHCl₃, 99.0%), titanium (III) chloride (TiCl₃), DETA (CP), anhydrous *n*-hexane (97%), and analytical grade NaCl, LiCl, and MgCl₂ were obtained from China National Pharmaceutical Group Industry Co., Ltd. (Beijing, China). All reagents and solvents were used as received, without further purification. Deionized (DI) water was used throughout the experiments.

A Neosepta AMX (Tokuyama Co., Japan) anion exchange membrane and a Selemion CSO (AGC Engineering Co., Japan) MCPM were used for electrodialysis (ED) experiments. Porous polyacrylonitrile (PAN), which was used as membrane substrate, was obtained from Guo Chu Technology Co., Ltd. (China).

2.2. Preparation of MOF nanoparticles

2.2.1. Preparation of UiO-66(Zr)-NH₂

ZrCl₄ (0.5 g) and 2-NH₂-BDC (0.536 g) were dissolved in DMF (60 mL), and then, concentrated HCl (percent assay of ~36.0%) (4 mL) was added to the solution. The mixture was sonicated for 20 min to fully dissolve all reagents and was subsequently heated at 80 °C for 24 h in an oven. The UiO-66(Zr)-NH₂ powder was collected via centrifugation and was alternately washed with DMF and CHCl₃ three times. The obtained nanoparticles were dried at 80 °C for 12 h.

2.2.2. Preparation of UiO-66(Zr/Ti)-NH₂

The as-prepared UiO-66(Zr)-NH₂ nanoparticles (0.09 g) were dispersed in DMF (60 mL) in an Al-wrapped vessel. Afterward, TiCl₃ (6.79 g) was added to the vessel and the mixture was heated at 85 °C under vacuum

for five days. The resulting UiO-66(Zr/Ti)-NH₂ powder was alternately washed with DMF and CHCl₃ three times.

For comparison, we used Ti⁴⁺ (TiCl₄ solution) to exchange Zr⁴⁺, and the prepared MOF was denoted UiO-66(Zr/Ti)-NH₂-Ti⁴⁺.

2.2.3. Preparation of TMC-UiO-66(Zr)-NH₂

UiO-66(Zr)-NH₂ powder (0.1 g) was added to 100 mL 0.1% (w/v) of a TMC/*n*-hexane solution, and the mixture was allowed to react for 60 min. Subsequently, the mixture was centrifuged, the powder was immersed in C₂H₅OH, and the system was magnetically stirred for 2 h. These steps were repeated three times to fully wash the residual impurities. The resulting powder was collected, dried at 80 °C for 12 h, and was further tested to confirm that TMC reacted with UiO-66(Zr)-NH₂.

2.3. Membrane preparation

2.3.1. HPAN membrane preparation

The PAN membranes were hydrolyzed by immersing them in a 1 M NaOH solution for 2 h followed by immersing them in a 1 M HCl solution for 12 h to acidify PAN. During the acidification process, the sodium carboxylate groups transformed into carboxylic acid groups. The hydrolyzed and acidified PAN membranes will be henceforth denoted as HPAN membranes. Subsequently, the prepared HPAN membranes were thoroughly washed with DI water.

2.3.2. Preparation of thin-film composite and nanocomposite membranes

All thin composite films on the HPAN membrane surface were obtained *in situ* using an interfacial polymerization route, as presented in Scheme 1. First, the HPAN membranes were immersed in a 1.0% (w/v) DETA aqueous solution. After 30 min, the membranes were pulled out of the solution and the excess DETA solution on them was removed using a rubber roller. Subsequently, UiO-66(Zr/Ti)-NH₂ powder was dispersed in a 0.1% (w/v) solution of TMC in *n*-hexane via ultrasonication for 1 h at 25 °C and was poured onto the surface of the amine-saturated HPAN substrate to react for 3 min. The obtained UiO-66(Zr/Ti)-NH₂-containing TFN membrane was denoted as TFN-(Zr/Ti) membrane. We fabricated TFN-(Zr/Ti)-1 and TFN-(Zr/Ti)-2 membranes with UiO-66(Zr/Ti)-NH₂ loadings of 0.01% and 0.03% (w/v) in 50 mL of *n*-hexane solution, respectively. For comparison, we also prepared thin-film composite (TFC) membranes that did not contain MOF nanoparticles and TFN-(Zr) membranes with UiO-66(Zr)-NH₂ nanoparticles. Using the same strategy, we fabricated TFN-(Zr)-1 and TFN-(Zr)-2 membranes with UiO-66(Zr)-NH₂ nanoparticle loadings of 0.01% and 0.03% (w/v), respectively. All MOF-based membranes were dried and subsequently stored in DI water for further use.

2.4. Characterization of MOF nanoparticles

2.4.1. Characterization of UiO-66(Zr)-NH₂ and UiO-66(Zr/Ti)-NH₂

The morphology of the UiO-66(Zr)-NH₂ and UiO-66(Zr/Ti)-NH₂ nanoparticles was analyzed using a Gemini 500 (Zeiss, Germany) scanning electron microscopy SEM instrument. A Nicolet Fourier-transform infrared FTIR spectrometer (Thermo Scientific, USA) was used to analyze the chemical structure of the nanoparticles. A TTR-III (Rigaku, Japan) X-ray diffraction (XRD) apparatus was used to obtain the XRD profiles of the samples. Synchrotron radiation photoelectron spectroscopy (SRPES) measurements were performed at the photoemission end-station of the BL10B beamline at the National Synchrotron Radiation Laboratory (Hefei, China). The N₂ adsorption-desorption isotherms of the nanoparticles were obtained using an Autosorb iQ (Quantachrome, USA) gas sorption analyzer at 77 K. Before testing, approximately 100 mg of MOF samples were activated via heating at 150 °C for 5 h under high vacuum. The zeta potentials of the nanoparticles were determined using a Zetasizer Nano ZS90 (Malvern, UK) device in DI water at pH 7.0.

The metal content (Zr, Ti) of the UiO-66(Zr/Ti)-NH₂ samples was determined using an Optima 7300DV (Perkin Elmer, USA) inductively coupled plasma-optical emission spectrometry (ICP-OES) system. Before

ICP-OES analysis, the nanoparticle samples were digested using a hydrofluoric acid solution and diluted with DI water.

2.4.2. Characterization of TMC-UiO-66(Zr)-NH₂

A Nicolet FTIR spectrometer (Thermo Scientific, USA) was used to analyze the chemical structure of TMC-UiO-66(Zr)-NH₂. The XRD spectra of the TMC-UiO-66(Zr)-NH₂ samples were obtained using a TTR-III (Rigaku, Tokyo, Japan) X-ray diffractometer. The elemental and chemical compositions of the TMC-UiO-66(Zr)-NH₂ samples were analyzed using an ESCALAB250 (Thermo Scientific, USA) X-ray photoelectron spectroscopy (XPS) instrument, and a 400 MHz (Bruker, Germany) proton nuclear magnetic resonance (¹H NMR) spectrometer, respectively.

2.5. Characterization of membranes

2.5.1. Characterization of membrane structure

The morphology of the membrane surfaces was characterized using a Gemini500 (Zeiss, Germany) SEM instrument. The cross-sectional morphology of the membranes was analyzed using a SU8220 (Hitachi, Japan) SEM apparatus. The chemical structure of the thin surface layers was studied using a Nicolet FTIR (Thermo Scientific, USA) spectrometer in attenuated total reflectance (ATR) mode. The cross-sections of the TFN-(Zr/Ti) membranes were further investigated using a JEM-2010 (JEOL, Japan) transmission electron microscopy (TEM) device. To prepare the membrane samples for TEM analysis, we embedded them in E44 epoxy resin. Subsequently, 100 nm thick sections of the membranes that were cut using an EM UC7 (Leica, Germany) ultramicrotome were transferred to a TEM grid. The roughness of the membrane surfaces was measured using a MultiMode V (Veeco, USA) atomic force microscopy (AFM) instrument.

2.5.2. Zeta potential measurements

The zeta potentials of the prepared membranes were measured using a SurPASS (Anton Paar Trading Co., China) electrokinetic instrument. Measurements were performed in the pH range of 3.0-7.0 in 1 mM aqueous KCl solution.

2.5.3. Current–voltage curves

The details of the method used to obtain the current–voltage (I–V) characteristic curves of the membranes are described in our previous paper.²⁸ Briefly, first, the membranes were equilibrated in the test solution for 24 h. All membranes were characterized using 0.5 M NaCl and 0.3 M Na₂SO₄ solutions as the test and electrode rinsing solutions, respectively. The test cell was connected to a HSPY-120-01 (Hanshengpuyuan Technology Co. Ltd., China) DC power supply *via* two Ti-coated ruthenium oxide electrodes. The current was incrementally increased and the changes in trans-membrane potential were recorded periodically (every 30-40 s) using a multimeter connected to Ag/AgCl electrodes.

2.5.4. Permselectivity measurements

The details of the ED performance of the membranes are described in our previous paper.²² Briefly, ED experiments were performed at a current density of 10 mA cm⁻². The selective layer faced the diluted chamber. First, 100 mL of 0.3 M Na₂SO₄ solution, 100 mL of a solution that contained 0.1 M NaCl (or 0.1 M LiCl) and 0.1 M MgCl₂, and 200 mL of a 0.01 M KCl solution were added to the electrode compartments, diluted chamber, and concentrated chamber, respectively. All solutions were circulated at flow rates of 86 mL min⁻¹ using peristaltic pumps. The ED tests were performed for 1 h. Samples were collected from the concentrated chamber for further analysis, and their ion concentrations were measured using ICP-OES.

Ion permeation through membranes ($J_{N^{n+}}$, mol cm⁻² s⁻¹), which measures the changes in the concentration of ions in the concentrated chamber, was calculated as follows:

$$J_{N^{n+}} = \frac{(C_t - C_0) \cdot V}{A_m \cdot t}, \quad (1)$$

where C_0 and C_t are the molar concentrations (M) of the ions (N^{n+}) in the concentrated chamber at the beginning ($t = 0$ min) and end ($t = 60$ min), respectively, of the ED test, V is the volume of solution in the concentrated chamber (200 mL), and A_m is the effective surface area of the membrane (7.07 cm^2).

The permselectivity was calculated using the following equation:

$$P_{M^+/D^{2+}} = \frac{J_{M^+} \bullet C_{D^{2+}}}{J_{D^{2+}} \bullet C_{M^+}}, \quad (2)$$

where J_{M^+} and $J_{D^{2+}}$ ($\text{mol cm}^{-2}\text{s}^{-1}$) are the permeations of monovalent and divalent cations, respectively, through the membrane after 60 min of testing and C_{M^+} and $C_{D^{2+}}$ (M) are the average concentrations of monovalent (Li^+ or Na^+) and divalent (Mg^{2+}) cations in the diluted chamber, respectively.

In this study, three sets of membranes were tested, and their separation performances were calculated as arithmetic averages. The testing device was thoroughly washed with DI water for 30 min after each test.

3. Results and discussion

3.1. Characterization of UiO-66(Zr)-NH₂ and UiO-66(Zr/Ti)-NH₂

The water stability of UiO-66(Zr)-NH₂ was tested by soaking its powder in water, and the XRD results confirmed the excellent stability of UiO-66(Zr)-NH₂ (Supporting Information, Figure S1). UiO-66(Zr/Ti)-NH₂ nanoparticles were produced *via* the post-synthetic exchange of Zr⁴⁺ ions with Ti³⁺ ions using a TiCl₃ solution. The SEM micrographs of UiO-66(Zr)-NH₂ and UiO-66(Zr/Ti)-NH₂ (Figures 1a and b, respectively) revealed that the size of their particles was approximately 60 nm. However, the post-synthetic ion exchange process rendered the surface of the UiO-66(Zr/Ti)-NH₂ particles relatively rough. The XRD patterns of UiO-66(Zr)-NH₂ and UiO-66(Zr/Ti)-NH₂ (Figure 1c) presented sharp and intense diffraction peaks without visible peak shifting, which confirmed the highly crystalline structure of the UiO-66(Zr)-NH₂ and UiO-66(Zr/Ti)-NH₂ nanoparticles. However, the intensities of the XRD peaks of UiO-66(Zr/Ti)-NH₂ were lower than those of UiO-66(Zr)-NH₂, which indicated the formation of defects during the post-synthetic process.³⁰ FTIR spectra were used to analyze the structure of the UiO-66(Zr)-NH₂ and UiO-66(Zr/Ti)-NH₂ nanoparticles. The negligible shifts of the characteristic FTIR peaks indicated that the post-synthetic process did not change the chemical structure of UiO-66(Zr)-NH₂ (Supporting Information, Figure S2). The N₂ adsorption-desorption isotherms (Figure 1d) indicated that the specific area of the nanoparticles increased from 764 m² g⁻¹ for UiO-66(Zr)-NH₂ to 1168 m² g⁻¹ for UiO-66(Zr/Ti)-NH₂, which further confirmed the changes in the properties of the MOF nanoparticles after the post-synthetic process. The pore size distributions of the UiO-66(Zr)-NH₂ and UiO-66(Zr/Ti)-NH₂ nanoparticles were calculated from the N₂ adsorption-desorption isotherms using the Saito-Foley (SF) and DFT models, and the results revealed the presence of inherent pores with sizes in the range of 7-11 Å in the MOF nanoparticles (Supporting Information, Figures S3 and S4, respectively). This pore size distribution enabled the facile permeation and sieving of the Na⁺, Li⁺, and Mg²⁺ ions, which presented hydrated diameters of 7.2, 7.6, and 8.6 Å, respectively.²⁹ The analysis of the SRPES profiles of the samples provided critical details on the post-synthetic process of the UiO-66(Zr)-NH₂ nanoparticles, such as the suppression of the Zr peak and emergence of the Ti peak (Figure 1e), which implied the successful replacement of Zr⁴⁺ ions with Ti³⁺ ions in UiO-66(Zr/Ti)-NH₂. To analyze the XPS profiles of the nanoparticles, we used Ti⁴⁺ ions to exchange a fraction of the Zr⁴⁺ ions in UiO-66(Zr)-NH₂ using the same post-synthesis process (Supporting Information, Figure S5). The 458.5 and 464.3 eV peaks in the Ti 2p XPS profile of UiO-66(Zr/Ti)-NH₂-Ti⁴⁺ were ascribed to Ti⁴⁺ 2p_{3/2} and Ti⁴⁺ 2p_{1/2}, respectively, (Supporting Information, Figure S5b). The SRPES profiles of UiO-66(Zr/Ti)-NH₂ in the Ti 2p region shows two new peaks at 457.8 eV and 463.6 eV, corresponding to Ti³⁺ 2p_{3/2} and Ti³⁺ 2p_{1/2}, respectively, revealing the coexistence of the Ti³⁺ and Ti⁴⁺ ions in the structure of UiO-66(Zr/Ti)-NH₂, and that was ascribed to the oxidation of TiCl₃ to TiCl₄ in air (Figure 1f). These results indicated the successful replacement of Zr⁴⁺ ions with Ti³⁺ ions in UiO-66(Zr/Ti)-NH₂. Furthermore, the Ti³⁺/Ti⁴⁺ molar ratio of UiO-66(Zr/Ti)-NH₂ was determined to be approximately 6:5. In addition, the post-synthetic process was monitored using ICP-OES,³¹ and the results indicated that the Ti/Zr molar ratio of UiO-66(Zr/Ti)-NH₂ was 9:4. Moreover, the zeta potentials of the UiO-66(Zr)-NH₂ and UiO-66(Zr/Ti)-NH₂ nanoparticles were tested (Supporting Information, Table S1). The decrease in zeta potential from 42.5 for UiO-66(Zr)-NH₂ to

31.5 for UiO-66(Zr/Ti)-NH₂ confirmed the exchange of Zr⁴⁺ ions with Ti³⁺ ions and successful conversion of UiO-66(Zr)-NH₂ into UiO-66(Zr/Ti)-NH₂.

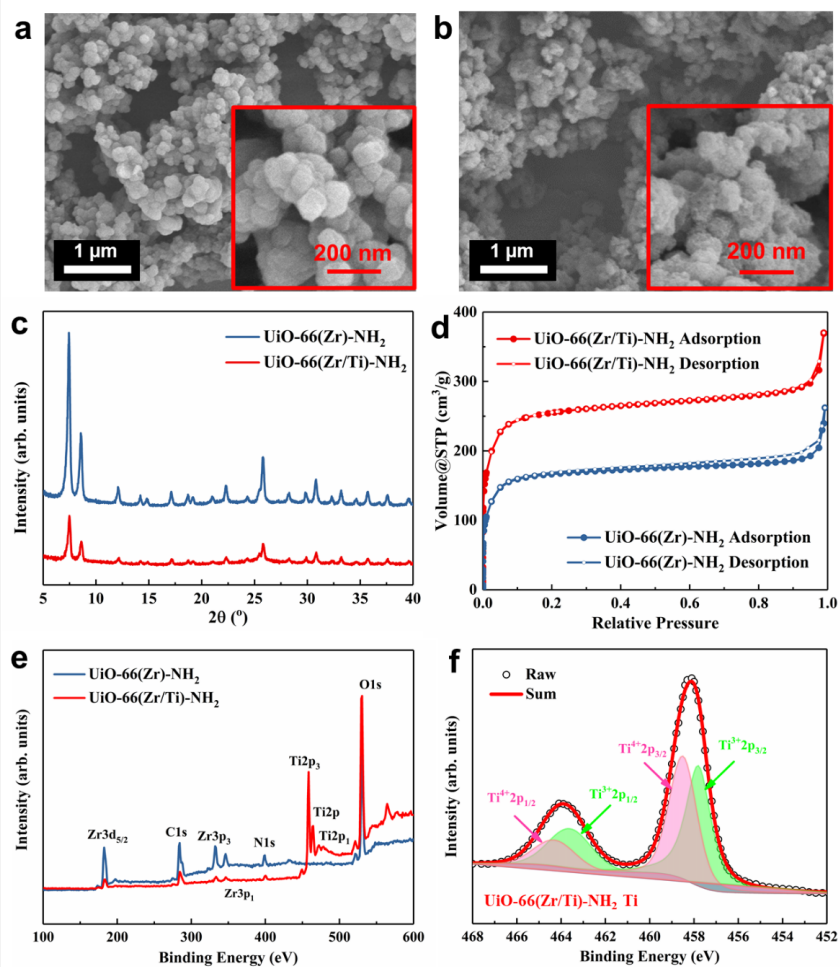


Figure 1. Scanning electron micrographs of the (a)UiO-66(Zr)-NH₂and (b)UiO-66(Zr/Ti)-NH₂nanoparticles. (c) X-ray diffraction patterns of UiO-66(Zr)-NH₂ and UiO-66(Zr/Ti)-NH₂. (d) N₂ adsorption–desorption isotherms of UiO-66(Zr)-NH₂ and UiO-66(Zr/Ti)-NH₂. (e) X-ray photoelectron spectroscopy (XPS) patterns of UiO-66(Zr)-NH₂ and UiO-66(Zr/Ti)-NH₂. (f) Ti 2p XPSspectra of UiO-66(Zr/Ti)-NH₂.

3.2. Reaction between TMC and UiO-66(Zr)-NH₂

When UiO-66(Zr)-NH₂ was mixed with TMC in *n*-hexane solution, covalent bonds formed between the amino groups of UiO-66(Zr)-NH₂ and acyl chloride groups of TMC.³²⁻³⁴ These bonds led to the formation of a uniform and sturdy surface layer that contained MOF nanoparticles affixed in the polyamide matrix. The formed covalent bonds were identified in the XPS profiles of TMC-UiO-66(Zr)-NH₂ (Figure 2). The peaks at 284.8, 286.5, and 288.7 eV in the C 1s XPS profile of UiO-66(Zr)-NH₂ corresponded to the C–C, C–N, and O=C–O bonds, respectively (Figure 2a).^{32, 33} The intensity of the characteristic peak of the C–N bond in the XPS spectra of TMC-UiO-66(Zr)-NH₂ was significantly higher than that in the XPS spectra of UiO-66(Zr)-NH₂ (Figure 2b). This indicated the formation of C–N bonds during the reaction of UiO-66(Zr)-NH₂ with TMC. The N 1s XPS profile of UiO-66(Zr)-NH₂ presented a single peak at 399.5 eV, which was

ascribed to the -NH_2 groups (Figure 2c). By contrast, an additional peak at 401.5 eV was observed in the N 1s spectra of TMC-UiO-66(Zr)- NH_2 , and that further confirmed the formation of O=C-N bonds during the reaction of UiO-66(Zr)- NH_2 with TMC (Figure 2d). The presence of the new peak at 1730 cm^{-1} in the FTIR spectrum of TMC-UiO-66(Zr)- NH_2 (Supporting Information, Figure S6a) also indicated the formation of covalent bonds between UiO-66(Zr)- NH_2 and TMC. Furthermore, the positions of the peaks in the XRD spectra of TMC-UiO-66(Zr)- NH_2 and UiO-66(Zr)- NH_2 did not change significantly, which indicated the negligible effect of the reaction on the crystal structure of UiO-66(Zr)- NH_2 (Supporting Information, Figure S6b). The ^1H NMR spectrum further confirmed that a reaction occurred between TMC and UiO-66(Zr)- NH_2 (Supporting Information, Scheme S1 and Figure S7). The covalent bonds that formed during the reaction tightened the interaction between UiO-66(Zr)- NH_2 and interfacial polymer layer.

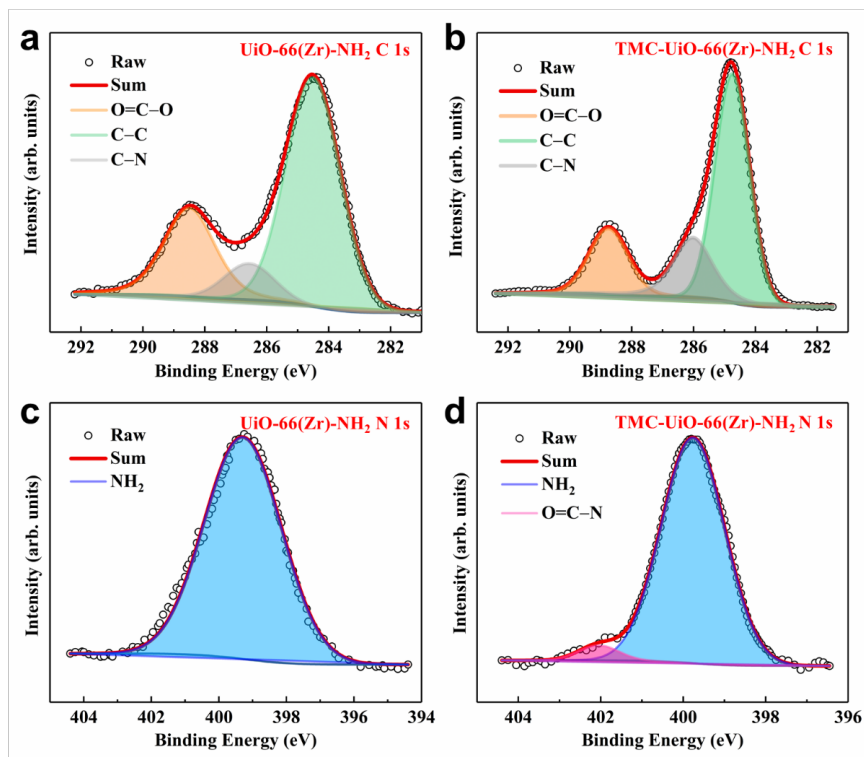


Figure 2. (a) and (b) C 1s and (c) and (d) N 1s X-ray photoelectron spectroscopy profiles of UiO-66(Zr)- NH_2 and TMC-UiO-66(Zr)- NH_2 , respectively.

3.3. Fabrication of the polyamide layer on the HPAN substrate

The surface and cross-sectional SEM images of the pristine HPAN porous substrate (Supporting Information, Figures S8a and b, respectively) revealed that the pores were uniformly distributed on the flat HPAN surface. In contrast, a continuous polyamide layer fully covered the HPAN substrate after the IP reaction (Supporting Information, Figures S8c and d) and formed TFC membranes. The SEM images of the TFN-(Zr)-1, TFN-(Zr/Ti)-1, TFN-(Zr)-2, and TFN-(Zr/Ti)-2 membrane surfaces (Figures 3a, b, c, and d, respectively) revealed their uniform morphology over large surface areas. Furthermore, the magnified SEM images of the membrane surfaces illustrated the uniform distribution of the ridge-and-valley structures of the nanocomposite membranes (Figures 3e-h). In addition, the formation of edges and corners within the surface MOF layers, which were caused by the crystal structure of the MOF particles, could be observed on the surfaces of the aforementioned membranes. The SEM cross-sectional images further illustrated the inverse relationship between the MOF loading and surface layer thickness, and revealed that the 100-200 nm MOF-loaded

nanocomposite layers (Figures 3i-l) were much thinner than the 250 nm pristine polyamide surface layers of the TFC membranes (Supporting Information, Figure S5d). The thickness of the surface layer decreased with increasing MOF loading (approximately 200 nm for the TFN-(Zr)-1 and TFN-(Zr/Ti)-1 membranes and approximately 100 nm for the TFN-(Zr)-2 and TFN-(Zr/Ti)-2 membranes). This suggested that the presence of the UiO-66(Zr)-NH₂ nanoparticles in the structure of the membranes hindered the diffusion of aqueous DETA toward the substrate, and thus, decreased the rate of the IP reaction.¹ The structure of the TFN-(Zr/Ti)-2 membrane with optimized UiO-66(Zr/Ti)-NH₂ loading was further analyzed using TEM. The results were in agreement with the cross-sectional SEM image in Figure 3l and further confirmed the presence of the UiO-66(Zr/Ti)-NH₂ nanoparticles (Supporting Information, dark regions in Figure S9) in the structure of the membrane.

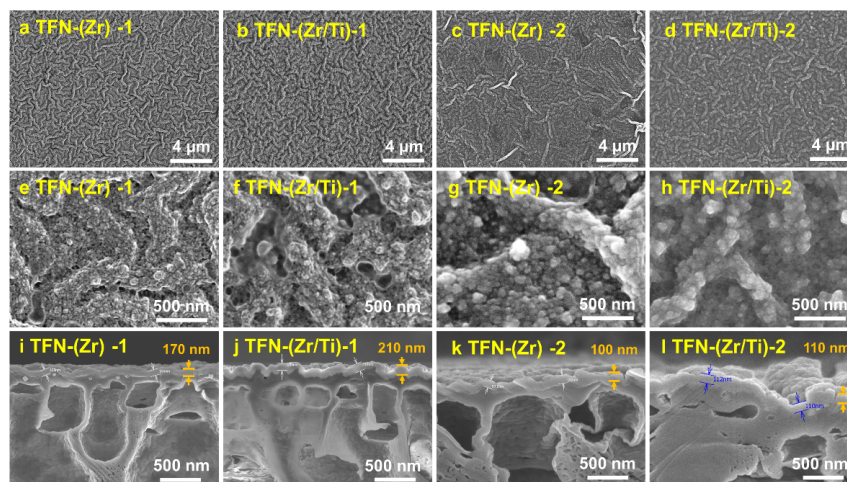


Figure 3. (a)-(d) Scanning electron microscopy (SEM) surface images, (e)-(h) magnified SEM surface images, and (i)-(l) cross-sectional SEM images of the metal-organic framework membranes in this study. Here TFN-(Zr)-1 and TFN-(Zr)-2 denote thin-film nanocomposite membranes with UiO-66(Zr)-NH₂ loadings of 0.01% and 0.03% (w/v) in 50 mL of *n*-hexane solution, respectively, and TFN-(Zr/Ti)-1 and TFN-(Zr/Ti)-2 denote thin-film nanocomposite membranes with UiO-66(Zr/Ti)-NH₂ loadings of 0.01% and 0.03% (w/v) in 50 mL of *n*-hexane solution, respectively.

In addition, the AFM morphology images of the aforementioned TFC and TFN membranes were obtained to visualize more topographic details and the measured surface roughness values, viz. their mean (Ra) and root mean square (RMS, Rq) roughness (Figure 4, Table 1, and Supporting Information, Figure S10). We determined that the Ra values of the TFN membranes were higher than those of the pristine TFC membrane (Ra = ±25.4).³⁵ Moreover, as the MOF nanoparticle loading increased, the Ra and Rq values of the TFN membranes decreased significantly, and that was attributed to the increase in the number of MOF nanoparticles that filled the ridge-and-valley structures. Furthermore, for the same MOF loading, the Ra and Rq values of the TFN-(Zr) membranes were relatively higher than those of the TFN-(Zr/Ti) membranes. That could be attributed to the surface of the UiO-66(Zr/Ti)-NH₂ nanoparticles being relatively rougher than that of the UiO-66(Zr)-NH₂ nanoparticles (Figure 1b). The increase in surface roughness after the incorporation of the MOF nanoparticles into membranes was highly beneficial and increased the exposed surface area for effective ion permeation.³⁶⁻³⁸ Thus, the precisely controlled symmetrical ridge-and-valley morphology and high surface roughness of the fabricated MOF membranes confirmed the merits of the adopted membrane fabrication strategy.

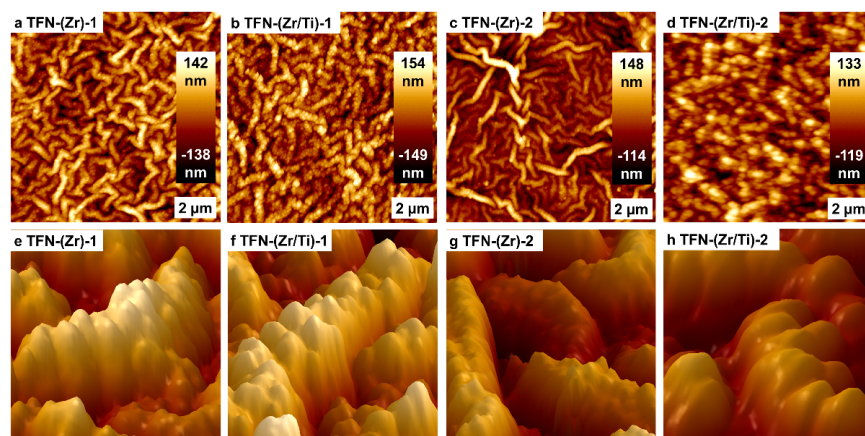


Figure 4.(a)-(d) Two- and (e)-(h) three-dimensional topographic atomic force microscopy images of the metal-organic framework-containing membranes in this study. Here TFN-(Zr)-1 and TFN-(Zr)-2 denote thin-film nanocomposite membranes with UiO-66(Zr)-NH₂ loadings of 0.01% and 0.03% (w/v) in 50 mL of *n*-hexane solution, respectively, and TFN-(Zr/Ti)-1 and TFN-(Zr/Ti)-2 denote thin-film nanocomposite membranes with UiO-66(Zr/Ti)-NH₂ loadings of 0.01% and 0.03% (w/v) in 50 mL of *n*-hexane solution, respectively.

Table 1. Mean (Ra) and root mean square (Rq) roughness values of the membranes in this study. Here TFC denotes thin-film composite membrane, TFN-(Zr)-1 and TFN-(Zr)-2 denote thin-film nanocomposite membranes with UiO-66(Zr)-NH₂ loadings of 0.01% and 0.03% (w/v) in 50 mL of *n*-hexane solution, respectively, and TFN-(Zr/Ti)-1 and TFN-(Zr/Ti)-2 denote thin-film nanocomposite membranes with UiO-66(Zr/Ti)-NH₂ loadings of 0.01% and 0.03% (w/v) in 50 mL of *n*-hexane solution, respectively.

Membrane	Ra (nm)	Rq (nm)
TFC	25.4	31.6
TFN-(Zr)-1	34.5	42.5
TFN-(Zr/Ti)-1	37.1	45.7
TFN-(Zr)-2	26.8	34.4
TFN-(Zr/Ti)-2	29.7	37.2

The ATR-FTIR spectra (Figure 5a) confirmed the successful embedding of the MOF nanoparticles into the TFN membranes. The presence of the characteristic bands of C=O (amide I) and N-H (amide II) at 1645 and 1550 cm⁻¹, respectively, in the ATR-FTIR spectra of the membranes confirmed the successful formation of a polyamide layer on the HPAN substrate. The increase in sharpness of the 1435 and 1260 cm⁻¹ peaks confirmed the successful UiO-66(Zr)-NH₂ or UiO-66(Zr/Ti)-NH₂ loading, respectively, during the IP reaction (Figure 5b). Furthermore, the additional peaks at 1255 and ~800 cm⁻¹, which were ascribed to the C-O bonds³⁹ and Zr-O clusters⁴⁰, respectively, further confirmed the formation of bonds between the UiO-66-NH₂ nanoparticles and polyamide layer on the surface of the HPAN substrate during the IP reaction. The fabricated TFC, TFN-(Zr)-2, and TFN-(Zr/Ti)-2 membranes were further analyzed using XPS, and the results confirmed the presence of UiO-66(Zr)-NH₂ or UiO-66(Zr/Ti)-NH₂ nanoparticles in the fabricated TFN membranes (Supporting Information, Figure S11). In addition, the zeta potentials of the TFN-(Zr)-1, TFN-(Zr)-2, TFN-(Zr/Ti)-1, and TFN-(Zr/Ti)-2 membranes at various pH values revealed that the surfaces of the TFN membranes were negatively charged at neutral pH, which is a requirement for the electrochemical cation permselective separation of both the Na⁺/Mg²⁺ and Li⁺/Mg²⁺ systems (Supporting

Information, Figure S12).

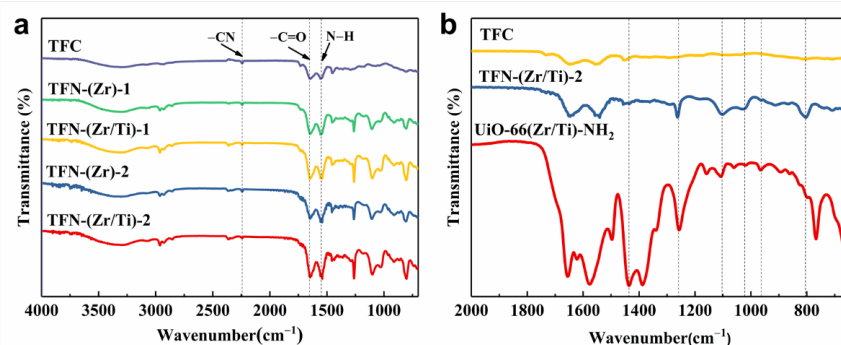


Figure 5. (a) Attenuated total reflectance Fourier-transform infrared spectra of TFC, TFN-(Zr)-1, TFN-(Zr/Ti)-1, TFN-(Zr)-2, and TFN-(Zr/Ti)-2 membranes. (b) Fourier-transform infrared spectra of TFC and TFN-(Zr/Ti)-2 membranes and UiO-66(Zr/Ti)-NH₂ nanoparticles. Here TFC denotes thin-film composite membrane, TFN-(Zr)-1 and TFN-(Zr)-2 denote thin-film nanocomposite membranes with UiO-66(Zr)-NH₂ loadings of 0.01% and 0.03% (w/v) in 50 mL of *n*-hexane solution, respectively, and TFN-(Zr/Ti)-1 and TFN-(Zr/Ti)-2 denote thin-film nanocomposite membranes with UiO-66(Zr/Ti)-NH₂ loadings of 0.01% and 0.03% (w/v) in 50 mL of *n*-hexane solution, respectively.

3.4. Electrochemical responses of the membranes under direct-current stimuli

The I-V curves are important for pre-evaluating the response of membranes, such as their resistance in the ohmic region (R_{or}) and limiting current density (LCD) under applied DC stimuli.⁴¹ The I-V curve of the commercial CSO membrane presents three regions. Conversely, the I-V curves of the TFC, TFN-(Zr), and TFN-(Zr/Ti) membranes were approximately linear up to the current density of 100 mA cm⁻² (Figure 6a). The linearity of the I-V curves indicated that the MOF-based membranes could be used at high current densities ([?]100 mA cm⁻²) and was attributed to the presence of nanochannels in the polyamide-containing MOF layers, which minimized the concentration polarization and facilitated the unhindered and continuous flow of ions. In this study, the R_{or} values of the membranes were calculated by inverting the slope of the I-V curves in the current density range of 0-10 mA cm⁻². The R_{or} of the TFN-(Zr/Ti)-2 membrane (30 Ω cm²) was lower than that of the TFN-(Zr/Ti)-1 membrane (33 Ω cm²) owing to the UiO-66(Zr/Ti)-NH₂ loading of the TFN-(Zr/Ti)-2 membrane being higher than that of the TFN-(Zr/Ti)-1 membrane (Figure 6b). Conversely, the absence of Ti³⁺ from the TFN-(Zr)-1 and TFN-(Zr)-2 membranes caused their R_{or} values to be higher (34 and 37 Ω cm², respectively) than those of the TFN-(Zr/Ti)-1 and TFN-(Zr/Ti)-2 membranes, which further confirmed the beneficial effects of the exchange of the Zr⁴⁺ ions with Ti³⁺ ions in the MOF layers. Consequently, the low R_{or} of the UiO-66(Zr/Ti)-NH₂ layers with well-defined ion transport channels facilitated the fast ion transportation, which is a highly desirable characteristic of energy-efficient membranes.

3.5. High cation permselective separation performance

A single laboratory-scale ED cell was used to evaluate the monovalent permselectivity of the prepared membranes in Na⁺-Mg²⁺ and Li⁺-Mg²⁺ mixed solutions. The TFC and TFN membrane surface layers with effective surface areas of 7.07 cm² were orientated facing the concentrated chamber, and testing was performed at a current density of 10 mA cm⁻². The cation permeation of all the membranes decreased as follows: Na⁺ > Li⁺ > Mg²⁺ (Figures 6c and d), which was in agreement with the diameters of the hydrated Na⁺ (0.72 nm), Li⁺ (0.76 nm), and Mg²⁺ (0.86 nm) ions. The increase in monovalent cation permeation through MOF-based membranes could be attributed to the additional ion transport channels of the MOF particles embedded in the MOF-containing surface layers. Moreover, the increase in the UiO-66(Zr)-NH₂

nanoparticle loading from 0.01% (w/v) for the TFN-(Zr)-1 membrane to 0.03% (w/v) for the TFN-(Zr)-2 membrane led to the further increase in J_{Na^+} from 5.32×10^{-8} to 6.35×10^{-8} mol $\text{cm}^{-2} \text{s}^{-1}$, respectively, and in J_{Li^+} from 4.65×10^{-8} to 5.26×10^{-8} mol $\text{cm}^{-2} \text{s}^{-1}$, respectively. In contrast (but consistent with the aforementioned reason), $J_{\text{Mg}^{2+}}$ decreased from 0.56×10^{-8} mol $\text{cm}^{-2} \text{s}^{-1}$ for the TFN-(Zr)-1 membrane to 0.48×10^{-8} mol $\text{cm}^{-2} \text{s}^{-1}$ for the TFN-(Zr)-2 membrane for the Na^+ - Mg^{2+} system and from 0.69×10^{-8} mol $\text{cm}^{-2} \text{s}^{-1}$ for the TFN-(Zr)-1 membrane to 0.43×10^{-8} mol $\text{cm}^{-2} \text{s}^{-1}$ for the TFN-(Zr)-2 membrane for the Li^+ - Mg^{2+} system. Consequently, the mono- over divalent cation separation performance of the TFN-(Zr) membranes, surpassed that of the TFC membrane, as illustrated in Figures 6c and d, for the Na^+ - Mg^{2+} and Li^+ - Mg^{2+} systems, respectively. In addition, the separation performance of the TFN-(Zr) membranes further improved with the increase in the MOF nanoparticle loading. Moreover, the separation performance of the TFN-(Zr) membranes for the Na^+ - Mg^{2+} system was higher than that for the Li^+ - Mg^{2+} system. That was ascribed to the diameter of the hydrated Na^+ ion being relatively smaller than those of the Li^+ and Mg^{2+} ions, which led to the slightly faster permeation of the Na^+ ions compared with the Li^+ and Mg^{2+} ions. The TFN-(Zr/Ti) membranes outperformed the TFN-(Zr) membranes in terms of cation permeation. J_{Na^+} of the TFN-(Zr/Ti)-2 membrane was 12.60% higher than that of the TFN-(Zr)-2 membrane. The higher cation permeation of the TFN-(Zr/Ti) membranes was attributed to the electrostatic assistance of the UiO-66(Zr/Ti)- NH_2 -containing ions separating surface layer. Consequently, the combined effect of physico-electrical such as size-sieving and electrostatic assistance in UiO-66(Zr/Ti)- NH_2 -containing membranes (particularly the TFN-(Zr/Ti)-2 membrane) caused J_{Na^+} and J_{Li^+} of the TFN-(Zr/Ti)-2 membrane to be 30% and 21% higher, respectively, and its $P_{\text{Na}^+/\text{Mg}^{2+}}$ and $P_{\text{Li}^+/\text{Mg}^{2+}}$ to be 3.8 and 5.1 times higher, respectively, than those of the standard state-of-the-art Selemion CSO (AGC Engineering Co., Japan) MCPM, and significantly higher than those of several recently reported permselective membranes (Supporting Information, Table S2). In addition, HPAN substrate membrane showed nearly no obvious selectivities for $\text{Na}^+/\text{Mg}^{2+}$ (~ 1.5) and $\text{Li}^+/\text{Mg}^{2+}$ (~ 1.3). Therefore, the excellent cation permselectivity could be attributed to the MOF-containing surface layers (Supporting Information, Figure S13). Because the changes in cation permeation and permselectivity of the TFN-(Zr/Ti)-2 membrane after five consecutive cation separation cycles were negligible, it was concluded that the representative TFN-(Zr/Ti)-2 membrane presented excellent stability (Supporting Information, Figure S14).

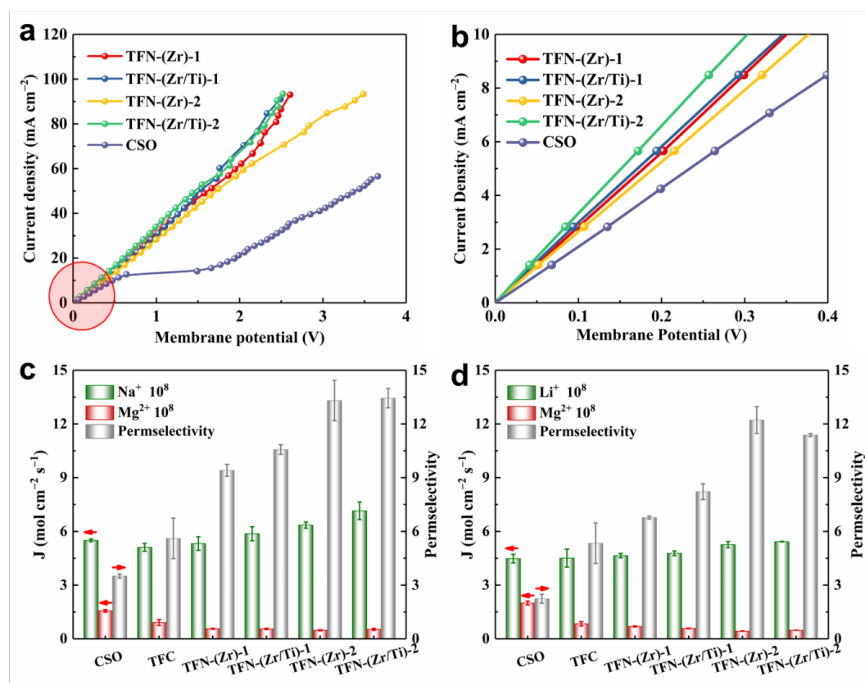


Figure 6. (a) Current density–membrane potential (I–V) curves of the TFN-(Zr)-1, TFN-(Zr/Ti)-1, TFN-(Zr)-2, TFN-(Zr/Ti)-2, and CSO membranes. (b) Magnified I–V curve of the area marked with a red circle in (a). Ion permeations (J) and permselectivities of the CSO, TFC, TFN-(Zr)-1, TFN-(Zr/Ti)-1, TFN-(Zr)-2, and TFN-(Zr/Ti)-2 membranes for the (c) Na^+ - Mg^{2+} and (d) Li^+ - Mg^{2+} systems at a current density of 10 mA cm^{-2} . Here TFC denotes thin-film composite membrane, TFN-(Zr)-1 and TFN-(Zr)-2 denote thin-film nanocomposite membranes with UiO-66(Zr)-NH_2 loadings of 0.01% and 0.03% (w/v) in 50 mL of n -hexane solution, respectively, and TFN-(Zr/Ti)-1 and TFN-(Zr/Ti)-2 denote thin-film nanocomposite membranes with $\text{UiO-66(Zr/Ti)-NH}_2$ loadings of 0.01% and 0.03% (w/v) in 50 mL of n -hexane solution, respectively.

4. Conclusion

Our results confirmed the formation of very uniform $\text{UiO-66(Zr/Ti)-NH}_2$ thin films on the surface of a HPAN substrate. The TFN membranes contained multidimensional subnanometer-sized ion transport channels, which were highly suitable for the simultaneous increase in cation permeation and ion-charge selectivity. Consequently, the TFN-(Zr/Ti)-2 membrane presented high monovalent ion fluxes ($J_{\text{Na}^+} = 7.15 \times 10^{-8} \text{ mol cm}^{-2} \text{ s}^{-1}$ and $J_{\text{Li}^+} = 5.43 \times 10^{-8} \text{ mol cm}^{-2} \text{ s}^{-1}$). Furthermore, the mono- over divalent cation separation performance of the TFN-(Zr/Ti)-2 membrane ($P_{\text{Na}^+/\text{Mg}^{2+}} = 13.44$ and $P_{\text{Li}^+/\text{Mg}^{2+}} = 11.38$) surpassed that of the TFC membrane. The high separation performance and outstanding stability during ED testing of the TFN membranes confirmed the benefits of the addition of $\text{UiO-66(Zr/Ti)-NH}_2$ nanoparticles to these membranes. In addition, the prepared TFN membranes presented high LCDs, which is a highly desirable characteristic for energy-efficient ion separation without unnecessary water splitting. Thus, the proposed strategy for the fabrication of $\text{UiO-66(Zr/Ti)-NH}_2$ -containing membranes and excellent permselective performance of the fabricated membranes could expand the large-scale use of MOFs for membrane applications.

Acknowledgement

The authors acknowledge the funding received from the National Natural Science Foundation of China (grant No. 21878282), Key Technologies R & D Program of Anhui Province (grant No. 17030901079) and the support of the Synchrotron-Radiation Joint Funds of University of Science and Technology of China (grant Nos. NSRLLHJJ2016 and UN2018LHJJ).

Notes

All authors contributed to the writing of the manuscript and approved the final version. ++ These authors contributed equally. Tingting Xu: conceptualization, investigation, methodology, writing-original draft and writing-review & editing. Fangmeng sheng: conceptualization, investigation, methodology, data curation, and writing-review & editing.

References

1. Conforti KM, Bazant MZ. Continuous ion-selective separations by shock electrodialysis. *AIChE J.* 2019.
2. Park HB, Kamcev J, Robeson LM, Elimelech M, Freeman BD. Maximizing the right stuff: The trade-off between membrane permeability and selectivity. *Science.* 2017; 356(6343).
3. Yang L, Tang C, Ahmad M, Yaroshchuk A, Bruening ML. High selectivities among monovalent cations in dialysis through cation-exchange membranes coated with polyelectrolyte multilayers. *ACS Appl. Mater. Interfaces.* 2018; 10(50): 44134-44143.
4. Abdu S, Marti-Calatayud M-Cs, Wong JE, Garcia-Gabaldon M, Wessling M. Layer-by-layer modification of cation exchange membranes controls ion selectivity and water splitting. *ACS Appl. Mater. Interfaces.* 2014; 6(3): 1843-1854.
5. Liu T-Y, Yuan H-G, Li Q, et al. Ion-responsive channels of zwitterion-carbon nanotube membrane for rapid water permeation and ultrahigh mono-/multivalent ion selectivity. *ACS Nano.* 2015; 9(7): 7488-7496.

6. Gao S, Zhu Y, Gong Y, Wang Z, Fang W, Jin J. Ultrathin polyamide nanofiltration membrane fabricated on brush-painted single-walled carbon nanotube network support for ion sieving. *ACS Nano*. 2019; 13: 5278-5290.
7. Kumar M, Tripathi BP, Shahi VK. Ionic transport phenomenon across sol-gel derived organic-inorganic composite mono-valent cation selective membranes. *J. Membr. Sci.* 2009; 340(1-2): 52-61.
8. Mahajan CV, Ganesan V. Influence of hydrogen bonding effects on methanol and water diffusivities in acid-base polymer blend membranes of sulfonated poly (ether ether ketone) and base tethered polysulfone. *J. Phys. Chem. B*. 2013; 117(17): 5315-5329.
9. Ge L, Wu L, Wu B, Wang G, Xu T. Preparation of monovalent cation selective membranes through annealing treatment. *J. Membr. Sci.* 2014; 459: 217-222.
10. Yang Y, Dementyev P, Biere N, et al. Rapid water permeation through carbon nanomembranes with sub-nanometer channels. *ACS Nano*. 2018; 12(5): 4695-4701.
11. Edri E, Aloni S, Frei H. Fabrication of core-shell nanotube array for artificial photosynthesis featuring an ultrathin composite separation membrane. *ACS Nano*. 2018; 12(1): 533-541.
12. Sadeghi I, Kronenberg J, Asatekin A. Selective transport through membranes with charged nanochannels formed by scalable self-assembly of random copolymer micelles. *ACS Nano*. 2017; 12(1): 95-108.
13. Li J-R, Sculley J, Zhou H-C. Metal-organic frameworks for separations. *Chem. Rev.* 2011; 112(2): 869-932.
14. Hua W, Zhang T, Wang M, Zhu Y, Wang X, Hierarchically structural PAN/UiO-66-(COOH)₂ nanofibrous membranes for effective recovery of Terbium (III) and Europium (III) ions and their photoluminescence performances, *Chem. Eng. J.* 2019; 370: 729-741.
15. Hu Z, Wang Y, Farooq S, Zhao D. A highly stable metal-organic framework with optimum aperture size for CO₂ capture. *AIChE J.* 2017; 63(9): 4103-4114.
16. Hou J, Hong X, Zhou S, et al. Solvent-free route for metal-organic framework membranes growth aiming for efficient gas separation. *AIChE J.* 2019; 65(2): 712-722.
17. Barankova E, Tan X, Villalobos LF, Litwiller E, Peinemann KV. A metal chelating porous polymeric support: The missing link for a defect-free metal-organic framework composite membrane. *Angew. Chem. Int. Ed.* 2017; 56(11): 2965-2968.
18. Qiu S, Xue M, Zhu G. Metal-organic framework membranes: from synthesis to separation application. *Chem. Soc. Rev.* 2014; 43(16): 6116-6140.
19. Denny Jr MS, Moreton JC, Benz L, Cohen SM. Metal-organic frameworks for membrane-based separations. *Nat. Rev. Mater.* 2016; 1(12): 16078.
20. Kwon HT, Jeong H-K. In situ synthesis of thin zeolitic-imidazolate framework ZIF-8 membranes exhibiting exceptionally high propylene/propane separation. *J. Am. Chem. Soc.* 2013; 135(29): 10763-10768.
21. Shamsaei E, Lin X, Low Z-X, et al. Aqueous phase synthesis of ZIF-8 membrane with controllable location on an asymmetrically porous polymer substrate. *ACS Appl. Mater. Interfaces*. 2016; 8(9): 6236-6244.
22. Xu T, Shehzad MA, Yu D, et al. Highly cation permselective metal-organic framework membranes with leaf-like morphology. *ChemSusChem*. 2019; 12(12): 2593-2597.
23. Katayama Y, Bentz KC, Cohen SM. Defect-free MOF-based mixed matrix membranes obtained by corona crosslinking. *ACS Appl. Mater. Interfaces*. 2019; 11: 13029-13037.

24. Liu T-Y, Yuan H-G, Liu Y-Y, Ren D, Su Y-C, Wang X. Metal-organic framework nanocomposite thin films with interfacial bindings and self-standing robustness for high water flux and enhanced ion selectivity. *ACS Nano*. 2018; 12(9): 9253-9265.
25. Zhang R, Ji S, Wang N, Wang L, Zhang G, Li JR. Coordination-driven in situ self-assembly strategy for the preparation of metal-organic framework hybrid membranes. *Angew. Chem. Int. Ed.* 2014; 53(37): 9775-9779.
26. Zhao C, Wang N, Wang L, et al. Functionalized metal-organic polyhedra hybrid membranes for aromatic hydrocarbons recovery. *AIChE J.* 2016; 62(10): 3706-3716.
27. Stock N, Biswas S. Synthesis of metal-organic frameworks (MOFs): routes to various MOF topologies, morphologies, and composites. *Chem. Rev.* 2011; 112(2): 933-969.
28. Shehzad MA, Wang Y, Yasmin A, et al. Biomimetic nanocones enable high ion permselectivity. *Angew. Chem. Int. Ed.* 2019; 58(36): 12776-12784.
29. Guo Y, Ying Y, Mao Y, Peng X, Chen B. Polystyrene sulfonate threaded through a metal-organic framework membrane for fast and selective lithium-ion separation. *Angew. Chem. Int. Ed.* 2016; 55(48): 15120-15124.
30. Kuwahara Y, Kango H, Yamashita H. Catalytic transfer hydrogenation of biomass-derived levulinic acid and its esters to γ -valerolactone over sulfonic acid-functionalized UiO-66. *ACS Sustain. Chem. Eng.* 2016; 5(1): 1141-1152.
31. Sun D, Liu W, Qiu M, Zhang Y, Li Z. Introduction of a mediator for enhancing photocatalytic performance via post-synthetic metal exchange in metal-organic frameworks (MOFs). *Chem. Commun.* 2015; 51(11): 2056-2059.
32. Zhang W, Wang S, Ji J, et al. Primary and tertiary amines bifunctional graphene oxide for cooperative catalysis. *Nanoscale*. 2013; 5(13): 6030-6033.
33. Yu X, Wang Z, Wei Z, et al. Novel tertiary amino containing thin film composite membranes prepared by interfacial polymerization for CO₂ capture. *J. Membr. Sci.* 2010; 362(1-2): 265-278.
34. Kalaj M, Denny Jr MS, Bentz KC, Palomba JM, Cohen SM. Nylon-MOF composites through postsynthetic polymerization. *Angew. Chem. Int. Ed.* 2019; 58(8): 2336-2340.
35. Firouzjaei MD, Shamsabadi AA, Aktij SA, et al. Exploiting synergetic effects of graphene oxide and a silver-based metal-organic framework to enhance antifouling and anti-biofouling properties of thin-film nanocomposite membranes. *ACS Appl. Mater. Interfaces*. 2018; 10(49): 42967-42978.
36. Navarro M, Benito J, Paseta L, Gascon I, Coronas Jn, Tellez C. Thin-film nanocomposite membrane with the minimum amount of MOF by the langmuir-schaefer technique for nanofiltration. *ACS Appl. Mater. Interfaces*. 2017; 10(1): 1278-1287.
37. Werber JR, Osuji CO, Elimelech M. Materials for next-generation desalination and water purification membranes. *Nat. Rev. Mater.* 2016; 1(5): 16018.
38. Jhaveri JH, Murthy Z. A comprehensive review on anti-fouling nanocomposite membranes for pressure driven membrane separation processes. *Desalination*. 2016; 379: 137-154.
39. Fei B, Chen C, Peng S, Zhao X, Wang X, Dong L. FTIR study of poly (propylene carbonate)/bisphenol A blends. *Polym. Int.* 2004; 53(12): 2092-2098.
40. Zhu X, Gu J, Wang Y, et al. Inherent anchorages in UiO-66 nanoparticles for efficient capture of alendronate and its mediated release. *Chem. Commun.* 2014; 50(63): 8779-8782.
41. Shehzad MA, Liang X, Yasmin A, et al. Angioplasty mimetic stented ion transport channels construct durable high-performance membranes. *J. Mater. Chem. A*. 2019; 7(16): 10030-10040.

Graphical abstract

